

Calibration of a Magnetic Field Probe as a Diagnostic for Laser-Produced Plasma

L. A. Morton^{1*}

¹ Carson-Newman College, Jefferson City, TN 37760

E. T. Everson^{2,†}, C. G. Constantin², D. Schaeffer², P. Pribyl², and C. Niemann²

² University of California Los Angeles, Los Angeles, CA 90095

Small, high speed B-dot probes were constructed and calibrated as instruments to detect the spontaneous magnetic field of laser-produced plasma, following established techniques. A network analyzer and oscilloscopes were used to diagnose the source of interference observed both in the calibration of the probes and in the laser-plasma measurements. Methods of reducing the interference were formulated, and tested when possible. A prototype analog integrator was also tested as a replacement for numerical integration of the probe signal. These improvements should allow more accurate magnetic field determinations for fast plasma phenomena using magnetic field probes.

PACS numbers:

I. INTRODUCTION

The magnetic field is an important property of a plasma, and knowledge of it is often needed to understand plasma behavior. There are varieties of ways to detect the magnetic field, but possibly the most straightforward diagnostic is the use of a simple loop or coil of wire. Faradays Law states:

$$V = -\frac{d\Phi_B}{dt} = -aN\frac{dB_{\perp}}{dt} \quad (1)$$

where Φ_B is the magnetic flux through the coil, B is the perpendicular component of the constant magnetic field strength over the area of a coil, a is the coil area, N is the number of turns in the coil, and V is the electromotive force or voltage. By measuring the voltage across the leads of a coil, the time-derivative of the magnetic flux through the coil can be determined. A B-dot probe is a plasma diagnostic instrument that takes advantage of this property. A B-dot probe usually consists of a single- or multi-turn coil mounted on or enclosed in a support that allows the coil to be inserted into or near the plasma. The term B-dot arises from the mathematical notation $\frac{dB}{dt} = \dot{B}$.¹ The magnetic field itself can be determined by integrating the B-dot signal in real-time by an analog integrator circuit^{2,3} or numerically after digitization of the signal.⁴⁻⁶

For several reasons B-dot probes must be calibrated to achieve accurate field measurements. Since probes tend to be small, physical measurements of the coil area are inaccurate.⁷ In addition, non-ideal electronic effects take place, especially involving the self-inductance of the coil or the cabling.⁸ Calibration is often accomplished by applying a known sinusoidal magnetic field from a Helmholtz coil driven by a signal generator and determining the amplitude of probes response as a function of frequency using an oscilloscope.⁹ Alternatively a network analyzer can be used, which simplifies data collection and allows the phase of the probe's response to be determined as well.^{6-8,10}

A. Probe Construction

For this report, probes were built using identical construction techniques as those described by Everson et al.⁶ The probe consists of two paired segments of magnet wire wrapped 5 times around each axis of a 3-axis heat-resistant plastic core, yielding coils of approximately 1 mm diameter. The core is placed at the tip of an alumina shaft and covered by a glass capillary tube. The leads from the loops are twisted into a bundle and run the 8" length of the hollow shaft, terminating in connections to six RG-178 coaxial cables. These carry the signal through the 3/8" stainless steel vacuum shaft and terminate in LEMO connectors that penetrate the vacuum seal (see Fig. 1).

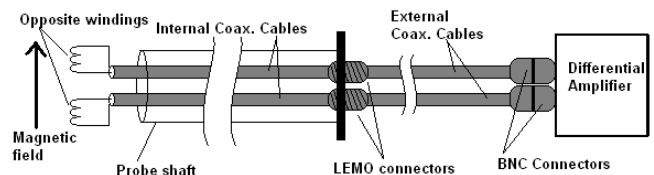
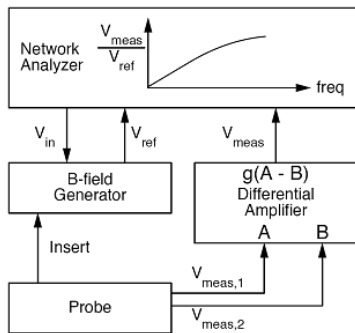


FIG. 1: Wiring illustration of probe

The two loops on each axis are connected to their respective cables in the opposite sense so that a changing magnetic flux will produce equal but opposite voltages from the two loops (Fig. 1). However, capacitive pickup will have the same polarity on each loop. Therefore, when the signals from the two loops are subtracted by the differential amplifier, the common capacitive induced signal will cancel, leaving the combined magnetically induced signal. Here $V_{meas,1}(t)$ and $V_{meas,2}(t)$ represent the opposite windings signals as functions of time, and $C(t)$ represents the common capacitive signal:

$$V_{meas,1}(t) - V_{meas,2}(t) = (\dot{B} + C(t)) - (-\dot{B} + C(t)) = 2\dot{B}(t) \quad (2)$$

FIG. 2: Calibration electronics. Reproduced from⁶

B. Current Probe Calibration Method

The B-dot probes calibration was also conducted following exactly following Everson et al⁶, with the omission of the probe testing via the oscillating test field produced by the RLC resonance circuit. The calibration electronics were assembled as shown in Fig. 2. The network analyzer (Agilent/HP E5100, 10kHz-180MHz) was set to display the real and imaginary part of the quantity V_{meas}/V_{ref} . Here V_{ref} is proportional to the current through the magnetic field generator and hence to the field strength. The ratio V_{meas}/V_{ref} represents the complex gain function of the probe/field-generator system.

The circuit of the probe tip was modeled as show in Fig. 3. Here C is the stray capacitance between the twisted leads, r is the resistance of the coils and leads, and R is the measuring resistance (50Ω). A pair of equations were derived which, when fitted to the gain and phase, yielded two calibration factors. The effective area of the probe coil can be calculated from aN , and $\tau_s = L/R$ reveals the coil's self-inductance.

A low-frequency calibration using a Helmholtz coil of 11 cm diameter was used to find aN via curve fitting the imaginary part of the following equation (Eq. 3) to the frequency data. Here ω is the frequency, and g is a factor that must be determined from the Helmholtz coil dimensions. Note that τ_s cannot be distinguished from τ , the cable delay, in the low frequency case.

$$\frac{V_{meas}(\omega)}{V_{ref}(\omega)} = aNg [(\tau_s + \tau)\omega^2 + i\omega] \quad (3)$$

The Helmholtz coil failed for high frequencies (above 1 MHz) so a straight wire segment was used as the field generator to collect high frequency data. This data was fitted to a more detailed equation to yield the factor τ_s :

$$\frac{V_{meas}(\omega)}{V_{ref}(\omega)} = \frac{\omega}{1 + (\omega\tau_s)^2} \{[\omega\tau_s \cos(\omega\tau) - \sin(\omega\tau)] + i[\omega\tau_s \sin(\omega\tau) + \cos(\omega\tau)]\} \quad (4)$$

Once the calibration factors were determined for each axis of a probe, these factors were applied as a first-order correction to the experimental data taken using

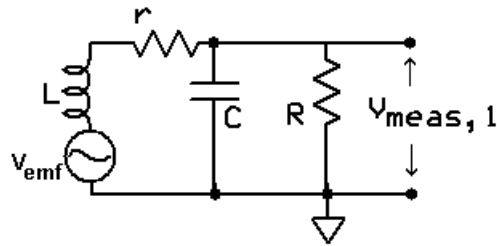


FIG. 3: Circuit of individual winding

the probe. This process was automated by an in-house software routine that also integrated the signal using the trapezoidal-sum method to yield the corrected magnetic field as a function of time (Eq. 5). Numerical integration was noted to be a potential source of error, as the integration compounds the measurement error at each step resulting in drift of the computed magnetic field from the actual field.

$$B(t) = \frac{1}{aN} \left[\int V_{meas}(dt) + \tau_s V_{meas} \right] \quad (5)$$

It was noted that the upper frequency limit for which the high-frequency model fit the calibration data was approximately 40 MHz, due to interference. This interference had been ascribed to pickup of the electromagnetic radiation from the test field by components of the probe other than the coils.⁶ The interference occurred for the new probes as well (Fig. 4).

Fig. 4 shows a typical plot of $|V_{meas}/V_{ref}|$ (known as the gain) as measured through the differential amplifier, illustrating the dips that constitute the interference. Fig. 5 shows the best theoretical fit to the gain using Eq. 4, up to 60 MHz for a single axis. Eq. 4 predicts an initially linear increase in the gain corresponding to the ideal case, Faraday's Law. The leveling-off of the curve is due to the increasing impedance of the self-induction of the probe coils as frequency is increased. The dips represent some

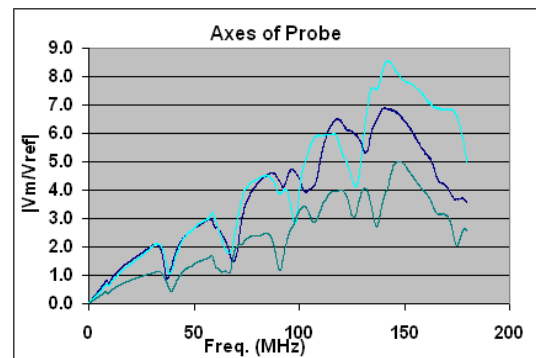


FIG. 4: Gain of each probe axis showing interference

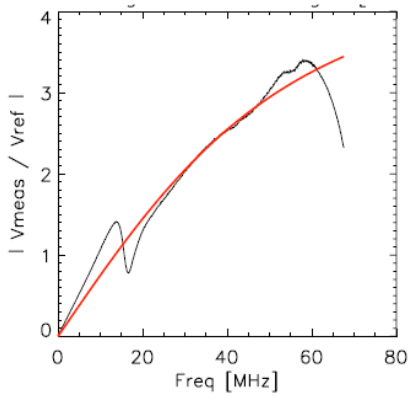


FIG. 5: Best fit to calibration by IDL routine

other frequency-dependent reduction in the gain.

This was the starting point for the current report. Other calibration procedures using network analyzers seem to have encountered similar interference,⁷⁻⁹ in one case at much higher frequency.¹ Experiments were conducted to determine and remove the source of the interference for this setup. An analog integrator was constructed and tested in hopes of eliminating numerical integration and its accompanying uncertainty from the data analysis. The probes and the integrator were tested by measuring the magnetic field of a laser-produced plasma. Interference was also seen in the experiment, and its source was traced.

II. B-DOT CALIBRATION REFINEMENT

It was concluded that electromagnetic interference from the magnetic source was not the cause, since the stray signal produced by positioning the wire segment B-field source at the midpoint of the alumina shaft or the steel shaft was not great enough in amplitude to cause such dips. Resonance of the inductance of the coil and the capacitance of the twisted leads was another possible cause. However, the required capacitance value calculated to create a resonance at the observed frequencies, given the known inductance of the probe coils ($\approx 2.5 \times 10^7 H$), is unrealistically large (hundreds of nanofarads).

Impedance mismatching was then investigated as a potential cause of the interference. For transmission lines such as coaxial cables, the cable has a characteristic impedance Z that is substantially constant for all frequencies and cable lengths. In order to avoid the creation of standing waves or echoes in the cable, the devices connected at either end must have the same impedance.¹¹ Otherwise, a signal traveling through the cable will be reflected at the mismatch. However, no signal should arrive at the probe coils, since they are the only source in the circuit. Thus, impedance matching has not been applied to B-dot probe coils in prior works.

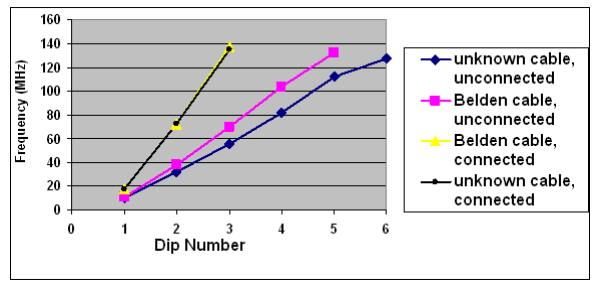


FIG. 6: Plot of frequency against dip number

The use of different cables and connection schemes demonstrated that the interference was cable-related. The dips were evenly spaced in frequency, and this spacing depended on the cable configuration. Two different sets of cable, differing in manufacturer and in length, but having the same impedance (50Ω) were used between the probe and the differential amplifier. For some tests electrical connection was made at the rear of the probe between the LEMO connectors of the two cables comprising a given axis (refer to Fig. 1). Shorting between the bodies of two of these connectors creates an electrical connection between the external conductors of the two cables. Fig. 6 shows the results of the four possible combinations of conditions. The interference is clearly cable-dependent.

The evidence suggests that there is reflection occurring where the external cables connect to the differential amplifier. Referring to Fig. 6, the frequency steps are smaller for the connected case. Since wavelength and frequency are inversely proportional, this indicates a short resonant cable length in the cross-connected case. This shorter length is independent of which external cable set was used; the scope traces were nearly identical. Thus, the resonance is taking place in the internal cables of the probe when the cross-connection is made. When the cross-connection is not made, the entire cable assembly resonates.

The external conductors of the cables are connected to the (grounded) metal housing of the differential amplifier. Making the cross-connection at the probe apparently moves the location of the reflection point. This implies that the connection at the differential amplifier is causing a reflection. No resonance could occur if the impedance mismatch were solely at the probe tip. Since the amplifier itself has 50Ω input impedance, the problem must lie with the BNC connectors on the cables. Replacing these cables should remedy the reflection problem and allow accurate calibration up to 150 MHz.

Impedance matching at the probe tip should also eliminate the interference by preventing the reflections moving away from the amplifier from being reflected back to the amplifier again. The resistance of a single coil was found to be $3-5 \Omega$, whereas the cable had an impedance of 50Ω . A test probe was built with a single 47Ω resistor added in series with each coil. Using the inductance L

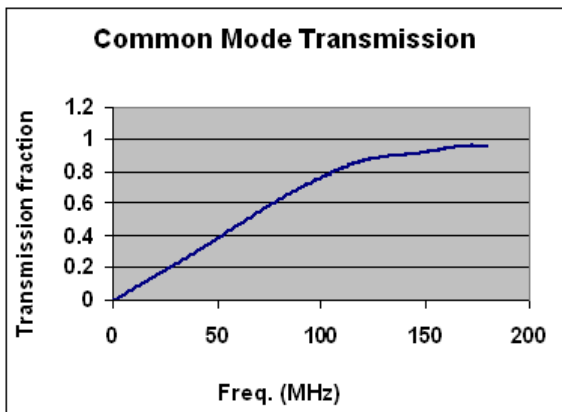


FIG. 7: Transmission of common mode through differential amplifier

calculated from the calibration, the impedance $|Z|$ of the probe should be less than 60Ω up to 100 MHz. The calibration test showed reduced resonance at low frequency (Fig. 8). However, the matched probe still retained interference but with dips spaced at higher frequencies. A better resistor choice would have been 40-45 Ω so that the impedance would remain closer to 50 Ω for a wider frequency range. The reason for the frequency-spacing change remains unclear. Note that the curvature of the matched probe trace is flatter: this is because the factor τ_s in Eq. 4 depends on R as well as L , and we have changed R .

An investigation of the individual windings independent of the differential amplifier was conducted. The individual windings had significantly less smooth frequency response than the combined signal from the differential amplifier. It seems that the differential amplifier was successfully removing a significant capacitive pickup from the field generator. The analysis of the calibration behavior would be simpler without the need to account for the interaction of the two windings and the amplifier. Unfortunately, the poor signal makes it impossible to distinguish any patterns without the use of the differential amplifier.

It was discovered that the differential amplifier quickly begins to transmit the undesired capacitive signal as frequency is increased, reaching 70 – 90% transmission by 100 MHz. Fig. 7 shows the transmission fraction as a function of frequency for one of the three channels of the amplifier. The poor common mode rejection seems to contradict the conclusion reached above, that the amplifier is removing significant capacitive effects during calibration. This may imply that the testing procedure used on the differential amplifier was faulty, or that the amplifier smooths out the signal only by some coincidental electronic fluke. If this test is accurate, however, a better differential amplifier may be called for if high-frequency capacitive pickup is expected from the plasma.

Although the calibration data was smoother with the LEMO connectors interconnected, they were left dis-

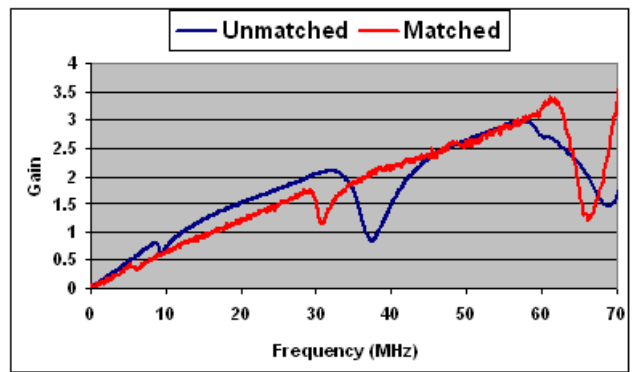


FIG. 8: Matched versus unmatched probe response, LEMOs not cross-connected

connected for the experiment for simplicity of analysis, since the cable behavior was not fully understood at the time. The calibration data for the disconnected case was used in analyzing the experimental data. Similarly, the impedance-matched probe was not considered suitably characterized for use in the measurement of the laser-produced plasma. It was also noted that for the normal probes, a decline in amplitude sets in at 150 MHz. However, the impedance-matched probe showed a similar decline starting at 100 MHz. The impedance-matched probe had been constructed with about twice the length of twisted leads as a normal probe. This would increase the shunting capacitance, which could cause such a decrease to occur at lower frequency.

III. INTEGRATOR

As previously mentioned, it was an objective of this work to produce a suitable analog integrator for fast B-dot signals, to replace the existing numerical integration. The circuit design shown in Fig. 9 was selected. It functions on the same principle as a classic Miller integrator¹¹ and has approximately the same response function (Eq. 6). It differs from the basic integrator in that a potentiometer is used to produce a variable voltage reference point to compensate for offsets in the input signal. The integration of a constant offset yields a linear voltage increase or decrease in time, resulting in saturation of the integrator.

$$V_{out} \approx -\frac{1}{RC} \int V_{in} dt \quad (6)$$

A prototype was tested using a LM741 operational amplifier integrated circuit (IC) with a gain-bandwidth product (GBWP) of 1 MHz. This integrator failed at 1 MHz, indicating that this circuit may be able to operate up to the GBWP of the amplifier IC. This circuit was also shown to operate well at frequencies as low as 1 kHz using an oscilloscope and signal generator. Fig. 10 shows the response of the integrator to a 1 kHz square wave: the

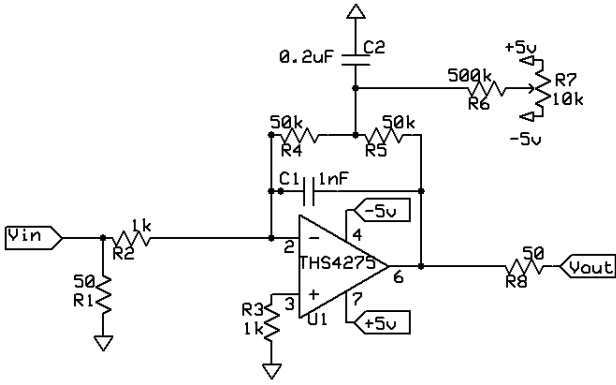


FIG. 9: Integrator schematic

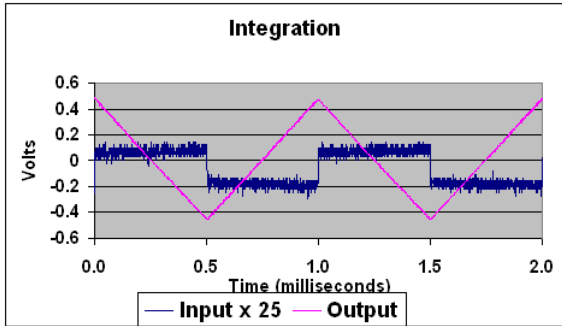


FIG. 10: 1kHz square wave input and integrator output

triangle wave is the integral of the square wave. No problems with saturation were encountered. The THS 4275 amplifier IC, with a GBWP of 1 GHz was used for the integrator. The higher frequency range of the integrator was tested using the network analyzer. In the frequency domain, the ideal Miller integrator has the response function:

$$V_{out} = \frac{-i}{\omega RC} \int V_{in} dt \quad (7)$$

This shows that a constant phase shift of 90° should be produced, and that the gain is inversely proportional to frequency. Fig. 11 shows a plot of the gain and Fig. 11 shows the phase difference. Note that the phase is initially 90° as desired, however due to cable length differences a constant time delay is introduced, which appears as a constant slope in the phase difference. The gain forms a nearly straight curve in the log-log plot, indicating that it is inversely proportional to frequency, as desired. The phase plot demonstrates that the integrator functioned as designed up to 150 MHz. However, this cutoff may be due to the loss of the signal in the noise floor, rather than a cessation of the integration function.

In testing, it was found that the baseline noise of the signal from the integrator was up to three times larger than that of the differential amplifier. Additionally, the single laser-plasma measurement taken with the integra-

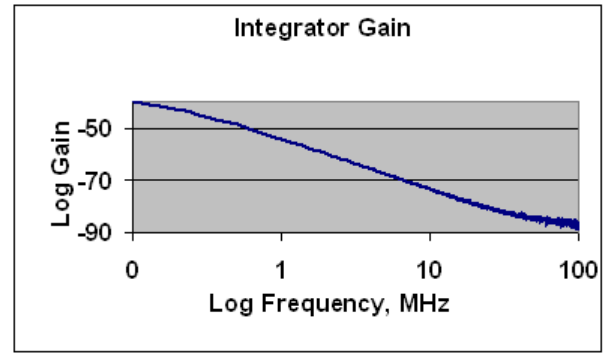


FIG. 11: Integrator gain

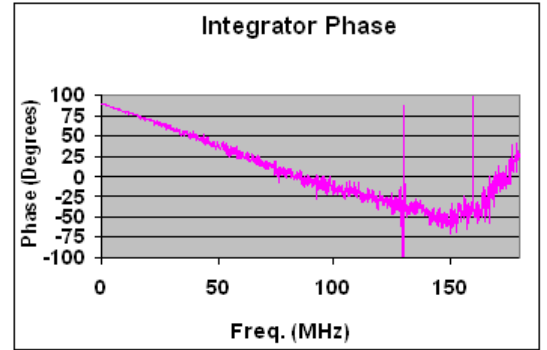


FIG. 12: Integrator phase difference

tor did not reveal any signal above this noise. It was subsequently discovered that the effective frequency content of the B-dot signals was at much higher frequency than the design point of the integrator, meaning that the gain was too low at these frequencies. Further work should focus on finding the correct gain and reducing noise by using better components and circuit board techniques.

IV. MEASUREMENT OF THE LASER-PRODUCED PLASMA

A. Experimental Arrangement

The functionality of the standard B-dot probe was tested in the working environment of the Small Target Chamber in the Phoenix Laser Laboratory. Fig. 12 shows the probe and target inside the chamber. The Phoenix laser was fired at graphite rod, producing a plasma jet that was directed toward the B-dot probe.

The Phoenix Laser is a long pulse (5 nanoseconds FWHM), high power (4 gigawatt) Nd:glass operating at 1064 nm wavelength. The laser capable of delivering 30 Joules with an intensity of up to 10^{14} W/cm², circularly polarized. It has energy stability of better than 10% and can fire once every three minutes. The laser struck the graphite target with a spot size $\approx 350\mu\text{m}$, for an esti-

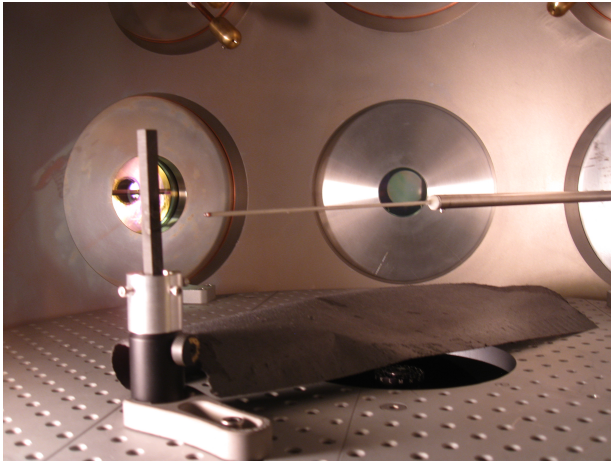


FIG. 13: Small Target Chamber interior showing target (left of center), probe (horizontal) and laser entrance window (behind target)

mated peak intensity 10^{12} W/cm², which should produce a plasma with an initial temperature of approximately 100 eV decreasing to 10 eV as the plasma expands.

The laser delivered 6-8 Joules to the target during this experiment. The beam struck the graphite at an angle of about 45° from normal to the surface. The graphite rod was 1 cm square and 6 cm tall, and was electrically isolated from the grounded chamber. The chamber was evacuated to 5×10^{-5} Torr by a turbo-pump. Chamber constraints dictated that the probe axis be misaligned by about 10° from the direction of the plasma flow. Thus varying the probe's distance from the target also resulted in lateral displacement of the probe relative to the plasma, complicating data interpretation.

The data from the probe was recorded by a digital oscilloscope (Tektronix Digital Oscilloscope 7254). An ICCD gated camera (Princeton Instruments PI-Max) was used with a CIII filter to image the laser-plasma from above at various times during the plasma expansion (Fig. 19). The images show that the probe was indeed in the path of the plasma. The ICCD images afford a rough initial velocity for the plasma of 240 km/s, which is in agreement with other laser-plasma velocities.¹⁴

The data from the probe seems to agree well with existing measurements of laser-produced plasma. Fig. 15 shows a raw B-dot signal overlaid with a diode signal which shows when the laser hit the target. Notice the high amplitude, high frequency noise initially, followed by the magnetic signal, and the lower-frequency, low-amplitude noise later. Fig. 16 shows the magnetic field derived from the integration and correction of the B-dot signal. Notice the noise amplitude is much lower, and that the field is initially negative but then becomes positive.

The magnetic field was found to always be strongest in the -Y direction (see axis in Fig. 14). Since the probe tip was slightly displaced radially, this is equivalent to

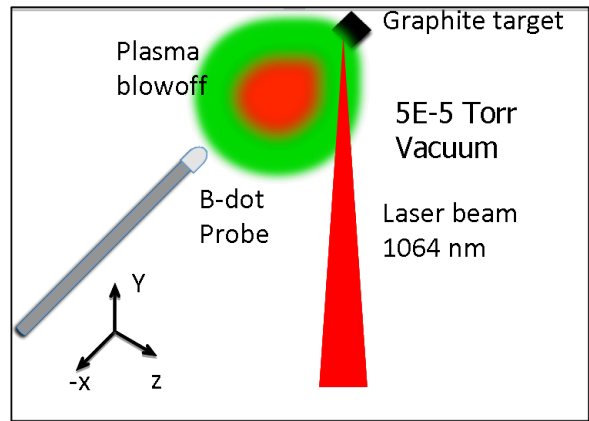


FIG. 14: Chamber layout viewed from above

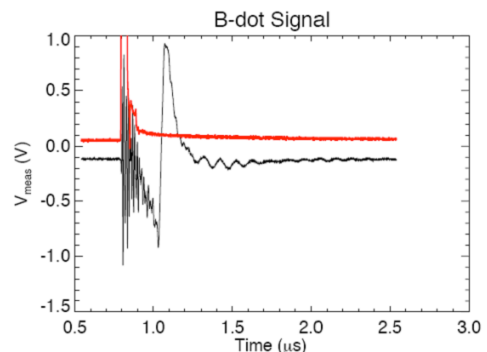


FIG. 15: Sample B-dot trace

the $-\theta$ direction in cylindrical coordinates where $+Z$ is the normal vector pointing in the direction of the plasma velocity. Such a field corresponds to an effective current in the $-Z$ direction, or into the target, as observed by others.^{4,12,14}

B. Results and Analysis

The peak-to-peak field strength (Fig. 18) seems to increase linearly with decreasing distance from the target;

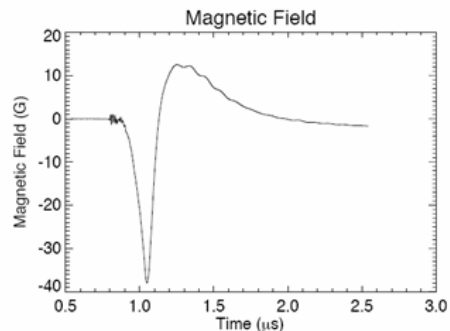


FIG. 16: Derived magnetic field trace

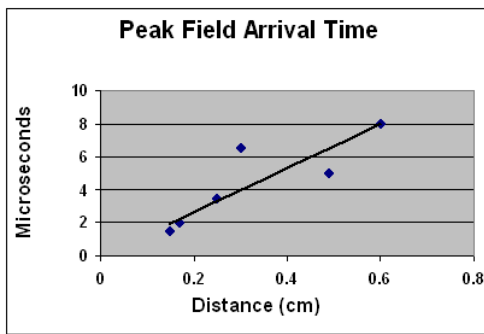


FIG. 17: Peak field arrival time versus distance

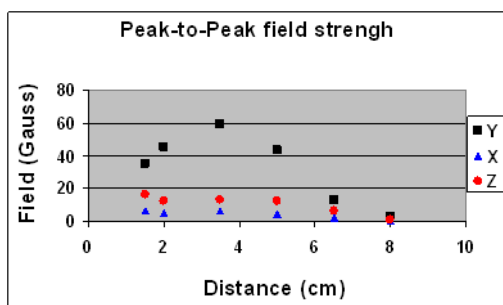


FIG. 18: Peak field strength versus distance

however, the last two points break this trend. This discrepancy may be due to inaccuracy of the probes radial placement, or the fact that the plasma (and hence field) is confined to a narrower radius at shorter distances from the target. Fig. 19 shows this effect: the plasma expands radially as it moves away from the target. The time delay between the laser firing and the peak magnetic field strength was determined and plotted against the distance of the probe from the target (Fig. 17). The slope of a linear fit to the data yields a speed of 140 km/s. This is in approximate agreement with the estimated 230 km/s initial plasma speed, and with the fact that the magnetic field is frozen into the laser-plasma and travels with it.

A reversed field is observed after the peak field has passed. Limited data from prior publications is available on the shape of the magnetic probe signals. Nakano and Sekiguchi, and Stamper et al, provide raw B-dot signal traces.^{12,14} Unexpectedly, both bear a remarkable similarity to the shape of the integrated data from this experiment. If the inductance of a B-dot probe is great enough, it is possible for the B-dot to act in self-integrating mode at high frequencies.^{1,9} However, this is not likely to be the case for the single-turn probe of Nakano and Sekiguchi. Some simulations and experiments do show that field reversal can occur.^{4,13} Since the numerical integration seems to be working properly on these data sets, the reversed field is considered to not to be an artifact.

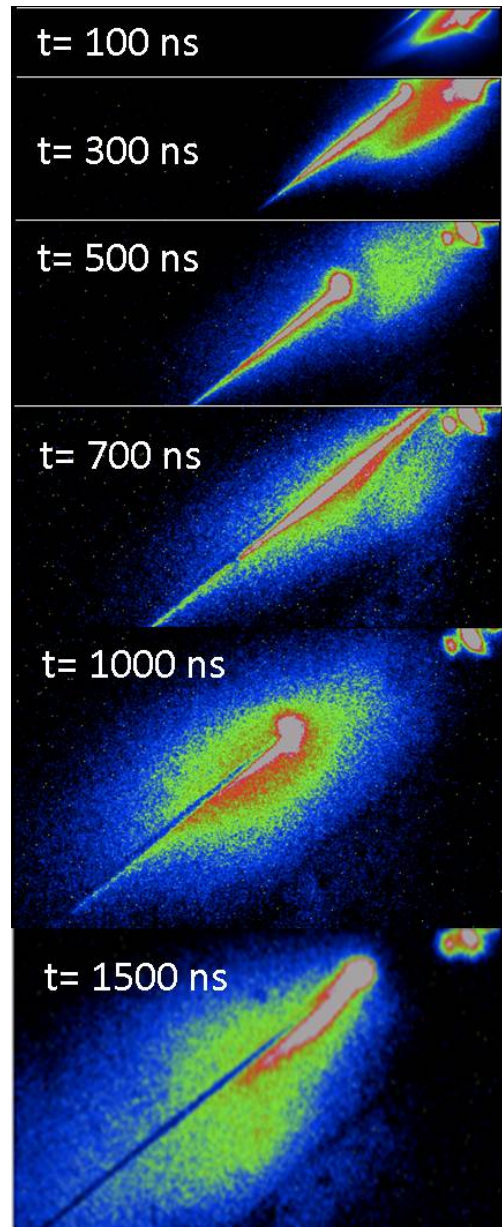


FIG. 19: Time evolution of plasma, from successive laser shots. Target is in top right corner, B-dot probe is the diagonal line. Note that the probe was translated between images

C. Evaluation of the Electronics

The numerical integration is relatively stable, especially when the amplitude of the actual B-dot signal is large. For traces with low B-dot signal (peak fields < 5 Gauss), the noise and integration error prevented accurate field readings. In most other cases the integrated magnetic field returned to a value close to zero, showing that the cumulative integration error for these magnetic field traces was small. While the voltage resolution is small (8-bit), the high sampling rate of the Tektronix oscilloscope (2.5 GS/s on each channel) is undoubtedly

responsible for the low error. However, even for some large-amplitude B-dot signals the integration does not return to zero. This makes a good case for the adoption of analog integration.

At early times electronics noise occurred in all the signals for which the laser beam struck the target, but did not occur when the laser was fired into a beam dump. The laser beam incident on the target apparently caused an electromagnetic pulse that resulted in ringing in some electronic component involved. The oscillations began simultaneously with the beams arrive, indicating that the plasma was not responsible for the pickup. Early in time, oscillations of 70-90 MHz occurred, but these died quickly, yielding an oscillation at 13 MHz. These oscillations can be seen in Fig. 15.

The signal from the differential amplifier showed evidence of a beat frequency. For one shot, traces were recorded of the two opposite windings from one axis, bypassing the differential amplifier. The traces show that the two windings are initially in phase, and of the same polarity, but with slightly different frequencies. As they shift out of phase, the differential amplifier does not cancel them. This is a shortcoming of the noise control method: the only way to clean up the signal is to prevent these oscillations from occurring. Some probe tips have been enclosed by grounded metal strips or foil, acting as Faraday cages.^{5,9} The fact that the interference observed happens at higher frequency than the magnetic signal is beneficial. When integrated, the amplitude of the oscillations is lower. (Recall from the integrator discussion that the gain of an integrator is inversely proportional to the signal frequency.)

V. SUMMARY

B-dot probes were constructed and calibrated following Everson et al. Interference occurring in the calibration process was traced to impedance mismatching and poor cable connections. Impedance matching of the probe was

shown to reduce this interference. This may be unnecessary if better cabling proves to resolve the issue. An analog integrator was constructed and characterized. With some refinement, this design should prove suitable for integrating fast probe signals. Future work should focus on reducing noise, and on finding an appropriate level of gain. Finally, a probe was tested in a laser-produced plasma and shown to provide useful data. The numerical integration routine appears to be functioning properly for most data sets. Stray oscillations occurred in the cabling. These oscillations were caused by a common mode voltage, indicating that the differential amplifier is not always sufficient to eliminate electrostatic effects. Improved shielding or grounding of the probe may be necessary. This work should prove valuable by increasing the accuracy of magnetic field measurements in fast plasma phenomena, especially laser-produced plasmas. In addition, the new probes constructed during this work are to be used during the upcoming experimental campaign of the UCLA High Energy Density Physics Group.

VI. ACKNOWLEDGMENTS

This work was supported by the National Science Foundation (NSF), the NSF REU Program at UCLA, and the DOE Partnership in Basic Plasma Physics. Thanks to my mentors Chris Niemann and Carmen Constantin for providing me with a great project and the advice and support to tackle it. Thanks also to my graduate student mentor Erik Everson for his patience and guidance. Thanks to Pat Pribyl and Mio Nakamoto for their generous assistance with the electronics. Thanks to Françoise Quval for making the REU Program such a great experience. Thanks to my advisor at CNC, Dr. Mike Seale, and to Dr. Henry Suters for their assistance and encouragement during the application process. Thanks also to Dr. Sean Cordry of CNC for a fruitful discussion about interpreting the interference data.

* Electronic address: lamorton@cn.edu

† Electronic address: eeverson@physics.ucla.edu;
URL: <http://hedp.physics.ucla.edu>

¹ P. Appelgren, C. Nylander, and S. E. Nyholm, FOI - Swedish Defense Research Agency Technical Report 1330-SE(2004).

² J.T. Slough and K. E. Miller, Rev. Sci. Instr. **72**, 417 (2001).

³ C. A. Romero-Talams, P.M. Bellan, and S. C. Hsu, Rev. Sci. Instr. **75**, 2664 (2004).

⁴ L.L. McKee, R. S. Bird, and F. Schwirzke, Phys. Rev. A **9**, 1305 (1974).

⁵ A. Vetushka and J.W. Bradley, J. Phys: Appl. Phys. **40**, 2037 (2007).

⁶ E.T. Everson, P. Pribyl, C. G. Constantin, A. Zylstra, D. Schaeffer, N. L. Kugland, and C. Niemann, Rev. Sci. Instr.

to appear.

⁷ M. P. Reilly, W. Lewis, and G. H. Miley, Rev. Sci. Instr. **89**, 053508 (2009).

⁸ S. Messer, D.D. Blackwell, W. E. Amatucci, and D. N. Walker, Rev. Sci. Instr. **77**, 115104 (2006).

⁹ R. C. Phillips and E. B. Turner, Rev. Sci. Instr. **36**, 1824 (1965).

¹⁰ J.G. Yang, J.H. Choi, B. C. Kim, N. S. Yoon, and S. M. Hwang, Rev. Sci. Instr. **70**, 3774 (1999).

¹¹ P. Scherz, Practical Electronics for Inventors (McGraw-Hill, 2007) pp. 278-81, 545.

¹² N. Nakano and T. Sekiguchi, J. Phys. Soc. Jap. **64**, 960 (1979).

¹³ O.V. Diyankov, I.V. Glazyrin, SV. Koshelev, and V. A. Likov, Laser and Particle Beams **18**, 255 (2000).

¹⁴ J. A. Stamper, K. Papadopoulos, R. N. Sudan, S. O. Dean,

E. A. McLean, and J. M. Dawson, Phys. Rev. Let. **26**, 1012 (1971).